

Excitonic Landscape of Monolayer Transition-Metal Dichalcogenides: Experimental Discrepancies, Theoretical Advances, and Strain Dependence

Cem Sevik,^{1,*} Purushothaman Manivannan,¹ Fulvio Paleari,^{2,†} and Milorad V. Milošević^{1,3,‡}

¹*COMMIT, Department of Physics and NANOLight Center of Excellence, University of Antwerp, Groenenborgerlaan 171, B-2020 Antwerp, Belgium*

²*Centro S3, CNR-Istituto Nanoscienze, I-41125 Modena, Italy*

³*Stavropoulos Center for Complex Quantum Matter, University of Notre Dame, Notre Dame, IN, USA*

(Dated: January 14, 2026)

Excitons in monolayer transition-metal dichalcogenides (TMDs) have garnered significant attention because of their large binding energies due to weakly screened Coulomb interaction, and direct bandgap at the K/K' point in the hexagonal Brillouin zone featuring spin-polarised bands due to spin-orbit coupling and lack of inversion symmetry. This makes them prospective for next-generation optoelectronic and quantum devices. However, despite the intense research activity, the reported values for exciton binding energies, quasiparticle gaps, and spectral features exhibit substantial variation across both experimental and theoretical studies. In this article, we present a comprehensive and critical assessment of the current understanding of excitonic properties in single-layer TMDs, integrating results from the angle-resolved photoemission spectroscopy (ARPES), photoluminescence (PL) measurements, and other experimental techniques with first-principles theoretical insights. Special emphasis is placed on the comparison and reconciliation of discrepancies observed across different experimental setups and sample qualities. Furthermore, we highlight our state-of-the-art GW-BSE calculations, which include both equilibrium and laterally strained systems, to systematically analyse the behaviour of direct and indirect excitons. By evaluating the effect of strain as a tunable control variable, we demonstrate its potential to engineer excitonic properties, supported by cross-validation against prior theoretical predictions and experimental findings. In doing so, we clarify the sources of discrepancies in the literature and offer a unified perspective on excited-state engineering strategies in two-dimensional TMDs.

I. INTRODUCTION

The advent of atomically thin two-dimensional (2D) materials has opened new frontiers in condensed matter physics, nanophotonics, and quantum optoelectronics by enabling precise control over electronic and optical properties at the atomic scale [1, 2]. Among these materials, monolayer transition metal dichalcogenides (TMDs) such as MoS₂, MoSe₂, WS₂, and WSe₂ have emerged as prototypical semiconductors due to their unique combination of a direct bandgap at the K-point and strong Coulomb interactions in reduced dielectric environments [3–7]. In addition, the strong spin-orbit coupling in the valence band combined with the lack of spatial inversion symmetry makes them crucial systems for valleytronics [8]. These features give rise to strongly bound excitons—quasiparticles formed by electron–hole pairs—with binding energies up to several hundred meV, robust enough to survive at room temperature and dominate the optical response [9–37]. These properties make monolayer TMDs prime candidates for next-generation light-emitting diodes, photodetectors, valleytronic devices, and quantum optical platforms [38–41].

Despite the rapid growth in experimental and the-

oretical efforts, substantial discrepancies persist across the literature concerning key excited-state properties—including quasiparticle gaps, exciton binding energies, and spectral peak positions. These variations arise from multiple sources such as sample quality, dielectric environment, substrate-induced screening, unintentional doping, and differences in experimental methodology [4–6, 42]. Additionally, the identification of bright (direct, spin-allowed) and dark (momentum- or spin-forbidden) excitons remains an open challenge, often requiring advanced spectroscopic tools and theoretical modeling to disentangle their signatures.

State-of-the-art many-body perturbation theory, particularly the GW approximation combined with the Bethe–Salpeter equation (GW-BSE), has played a central role in interpreting and predicting excitonic spectra in TMDs. These approaches have revealed rich and complex exciton landscapes that include hydrogenic Rydberg series, intervalley excitons, and phonon-assisted dark states [43–50]. Yet, even with these advanced frameworks, theoretical predictions often diverge in quantitative detail from one another and from experimental benchmarks.

Among external control parameters, strain engineering has emerged as a particularly powerful knob for modulating the band structure and excitonic interactions in single-layer 2D materials. Biaxial and uniaxial strain can reshape the relative energy positions of valleys (e.g., Γ , K, $\Lambda = \frac{1}{2}|\Gamma\mathbf{K}|$), modify effective masses and influence dielectric screening, leading to systematic shifts in exciton

* cem.sevik@uantwerpen.be

† fulvio.paleari@nano.cnr.it

‡ milorad.milosevic@uantwerpen.be; mmilosev@nd.edu

binding energies and direct–indirect exciton transitions [44, 51–55]. Experiments have demonstrated that even modest tensile strain (1–2%) can shift bright excitons by up to 100 meV and enable the optical activation of otherwise dark excitonic states [47, 56]. However, a unified, quantitative understanding of how strain affects different types of excitons across the family of monolayer TMDs remains incomplete.

In this article, we address these issues by providing a rigorous and comprehensive assessment of the excitonic properties of monolayer TMDs. We integrate high-precision GW–BSE calculations—performed with tightly converged parameters and including spin-orbit coupling—with an extensive review of literature, including ARPES, photoluminescence (PL), magneto-optical spectroscopy, and electron energy loss spectroscopy (EELS) experiments. Special emphasis is placed on systematically characterizing the evolution of direct and indirect excitons under biaxial strain in MoS₂, MoSe₂, WS₂, and WSe₂. We extract quantitative strain gauge factors and determine critical thresholds for direct-to-indirect transitions, offering an accurate framework that reconciles conflicting reports in the literature. Our goal is not only to discuss the origin of observed discrepancies, but also to interpret the use of strain as an exciton modulation strategy.

II. METHODS

The single-particle wavefunctions and corresponding energies used as input for the G₀W₀ and Bethe–Salpeter Equation (BSE) calculations were obtained from Kohn–Sham Density Functional Theory (DFT), as implemented in Quantum ESPRESSO (QE) [57]. These calculations employed fully relativistic, norm-conserving pseudopotentials within the generalized gradient approximation (GGA), using the Perdew–Burke–Ernzerhof (PBE) exchange–correlation functional [58, 59]. The pseudopotentials were sourced from the PseudoDojo project [60].

The pseudopotentials included semi-core electrons, with valence configurations of 4s²4p⁶5s¹4d⁵ for molybdenum, 5s²5p⁶6s²5d⁴ for tungsten, 3s²3p⁴ for sulfur, and 3d¹⁰4s²4p⁴ for selenium. Spin-orbit coupling (SOC) effects were fully included through spinorial wavefunctions. A plane-wave energy cutoff of 120 Ry was used, along with a symmetric Monkhorst–Pack *k*-point grid of (42×42×1) (169 *k*-points in the irreducible Brillouin zone, centered at Γ) for all materials.

To eliminate spurious interlayer interactions, a vacuum layer of 60 Bohr was added along the out-of-plane direction, and a 2D Coulomb truncation scheme was applied [61]. van der Waals (vdW) interactions were incorporated using Grimme’s D2 dispersion correction [62, 63]. All calculations were repeated for biaxial strain values ranging from -1.5% to +1.5%, keeping the computational parameters fixed. For each strain value, full ionic relaxation was included.

The Many-Body Perturbation Theory (MBPT) calculations were performed using the YAMBO code [64, 65], with the DFT wavefunctions and energies as input. A 2D slab geometry was employed for truncating Coulomb interactions [66, 67]. The G₀W₀ corrections to the quasiparticle energies were calculated using the Godby–Needs plasmon-pole approximation for the dynamically screened interaction [68, 69]. Convergence of both direct and indirect band gaps was ensured using 500 bands for the screened Coulomb potential *W* and 600 bands for the Green’s function *G*, with screening computed within the Random Phase Approximation (RPA). These corrections were applied to the top four valence bands and the bottom four conduction bands.

The Bethe–Salpeter Equation (BSE) for excitonic states was solved within the Tamm–Dancoff approximation (uncoupled resonant and antiresonant transitions), [70, 71]. The resulting BSE two-particles Hamiltonian, $H^{BSE}(\mathbf{Q})$, describes the coupling of single-particle transitions with momentum difference $\mathbf{k}_1 - \mathbf{k}_2 = \mathbf{Q}$, mediated by electron–hole Coulomb interactions. These interactions are approximated as the sum of the direct Hartree (*H*) and statically screened exchange (SEX) terms [72]:

$$H_{c_1 v_1 \mathbf{k}_1}^{BSE}(\mathbf{Q}) = (\epsilon_{c_1 \mathbf{k}_1} - \epsilon_{v_1 \mathbf{k}_1 - \mathbf{Q}}) \delta_{c_1 v_1 \mathbf{k}_1}^{c_2 v_2 \mathbf{k}_2} + (f_{v_2 \mathbf{k}_2} - f_{c_2 \mathbf{k}_2}) \Xi_{c_1 v_1 \mathbf{k}_1}^{HSEX}(\mathbf{Q}). \quad (1)$$

Here, ϵ_{nk} refers to a quasiparticle energy in the GW approximation, with occupation number f_{nk} .

Accordingly, the electron–hole kernel is composed by two contributions coming from the two pieces of the interaction:

$$\Xi_{c_1 v_1 \mathbf{k}_1}^{HSEX}(\mathbf{Q}) = -W_{c_1 v_1 \mathbf{k}_1}^{SEX}(\mathbf{Q}) + V_{c_1 v_1 \mathbf{k}_1}^H(\mathbf{Q}), \quad (2)$$

with W^{SEX} representing the attractive screened interaction (responsible for the exciton binding) and V^H being the repulsive, unscreened exchange interaction. The latter term is zero for triplet excitons because of how it couples electronic wavefunctions (singlet excitons are the only ones that may be excited optically).

Exciton energies $E_\lambda(\mathbf{Q})$ and corresponding wavefunctions were obtained by diagonalizing the BSE Hamiltonian for each center-of-mass (COM) momentum \mathbf{Q} :

$$\sum_{c_2 v_2 \mathbf{k}_2} H_{c_1 v_1 \mathbf{k}_1}^{BSE}(\mathbf{Q}) A_{c_2 v_2 \mathbf{k}_2}^{\lambda \mathbf{Q}} = E_\lambda(\mathbf{Q}) A_{c_1 v_1 \mathbf{k}_1}^{\lambda \mathbf{Q}}. \quad (3)$$

Here, $A_{cv \mathbf{k}}^{\lambda \mathbf{Q}} = \langle c \mathbf{k} \otimes v \mathbf{k} - \mathbf{Q} | \lambda \mathbf{Q} \rangle$ represent the projections of the excitonic eigenvectors onto the electron–hole product states for a transition from valence band *v* with momentum $\mathbf{k} - \mathbf{Q}$ to a conduction band *c* with momentum \mathbf{k} . These coefficients describe the transformation from the single-particle transition basis to the excitonic basis in which $H^{BSE}(\mathbf{Q})$ is diagonal. As demonstrated in Sec. II A 3, the dominant influence of strain stems from modifications to the single-particle states $|c \mathbf{k}\rangle$ and $|v \mathbf{k}\rangle$.

To characterize the momentum-space distribution of excitonic states, we analyzed the k -resolved exciton weights at a chosen state λ and momentum \mathbf{Q} , defined as,

$$\mathcal{W}^{\lambda\mathbf{Q}}(\mathbf{k}) = \sum_{vc} \left| A_{vc\mathbf{k}}^{\lambda\mathbf{Q}} \right|^2, \quad (4)$$

providing a direct measure of the exciton's distribution across the Brillouin zone. Peaks in $\mathcal{W}^{\lambda}(\mathbf{k})$ indicate the dominant regions in reciprocal space contributing to a given excitonic state, enabling classification according to their character and transfer momentum, such as $K-K$ ($\mathbf{Q} = 0$), $K-\Lambda$ ($\mathbf{Q} = \Lambda$), or $\Gamma-K$ ($\mathbf{Q} = \mathbf{K}$).

Moreover, we define the exciton binding energy as the difference between the exciton energy and the corresponding minimum quasiparticle gap *at the same momentum transfer vector*:

$$E_b(\lambda; \mathbf{Q}) = E_{\lambda}(\mathbf{Q}) - \min_{vc\mathbf{k}} \{ \epsilon_{c\mathbf{k}} - \epsilon_{v\mathbf{k}-\mathbf{Q}} \} \quad (5)$$

Finally, the optical absorption spectrum including excitonic effects is given by the imaginary part of the 2D polarizability $\alpha(\omega)$ (which is related to the macroscopic dielectric function[73]) computed at the BSE level:

$$\alpha_2(\omega) = \frac{2\pi}{A} \sum_{\lambda} \left| \boldsymbol{\epsilon} \cdot \sum_{cv\mathbf{k}} A_{cv\mathbf{k}}^{\lambda 0} \mathbf{d}_{cv\mathbf{k}} \right|^2 \delta_{\eta}(\omega - E_{\lambda}(\mathbf{0})). \quad (6)$$

Here, $\mathbf{d}_{cv\mathbf{k}}$ is the single-particle interband dipole matrix element, $\boldsymbol{\epsilon}$ the polarization direction of the incoming light, and A the 2D unit cell area. η is a numerical broadening parameter expanding the delta functions into Lorentzian peaks.

A. Results

1. Electronic properties: Strain-free

The distinctive band structure of monolayer TMDs, particularly the energy separations between key high-symmetry points in the Brillouin zone, plays a critical role in determining the nature and energetics of both direct and indirect excitons in these materials. Specifically, the energy difference between the highest valence states at K and Γ , defined as $\Delta E_{\text{K}\Gamma}^v = E_{\text{K}}^v - E_{\Gamma}^v$, and the separation between the lowest conduction states at K and Λ , $\Delta E_{\text{K}\Lambda}^c = E_{\text{K}}^c - E_{\Lambda}^c$, are pivotal in shaping the excitonic landscape. As illustrated in Figure 1, the band structures calculated without many-body corrections (MBCs) fail to reproduce these energy differences with sufficient accuracy, thereby limiting the reliability of excitonic predictions.

For example, the calculated conduction-band offset $\Delta E_{\text{K}\Lambda}^c$ shows strong method dependence, varying by more than 150 meV in sulfur-based compounds and by approximately 85 meV in selenium-based compounds

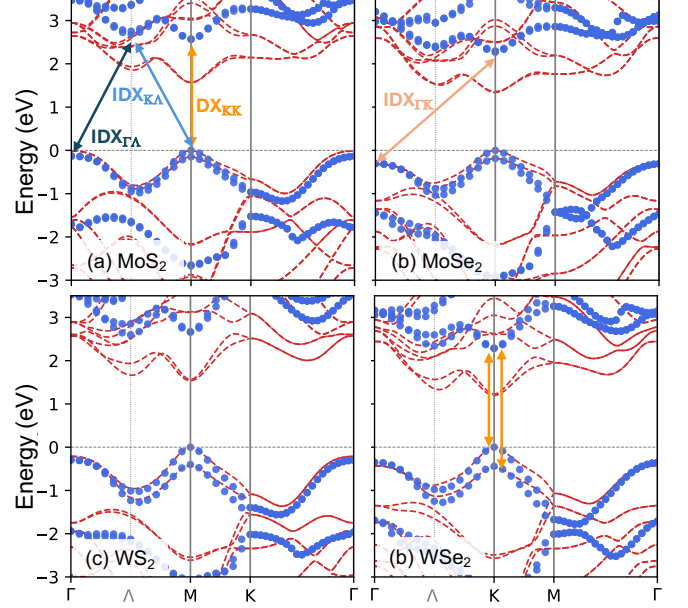


FIG. 1. The calculated PBE (dashed red lines) and G_0W_0 (blue symbols) band structure of (a) MoS_2 , (b) MoSe_2 , (c) WS_2 , (d) WSe_2 .

(see Table I) comparing PBE and GW approaches. Similarly, the inclusion of MBCs significantly alters the calculated $\Delta E_{\text{K}\Gamma}^v$. Such deviations directly reshape the overall excitonic landscape. Collectively, these observations highlight the critical importance of many-body corrections in accurately capturing the excitonic properties of these materials, in agreement with previous many-body studies [24, 43, 74, 75].

Strikingly, many-body effects induce appreciable shifts not only in the conduction band states but also in the deeper valence states, which are primarily composed of chalcogen p -orbitals [44, 76]. While these modifications do not directly influence the low-energy excitonic states of primary interest, they underscore the broader impact of many-body interactions on the electronic and optical properties of TMDs, including those with metallic character.

In discussing the role of MBCs, it is also critical to emphasize the importance of computational accuracy. Parameters such as the choice of pseudopotentials, plane-wave energy cutoffs, and k -point sampling significantly affect the resulting electronic structure, quasiparticle energies, and excitonic states in both G_0W_0 and BSE calculations. For instance, previously reported DFT (GW) band gap values span 1.58–1.89 eV (2.41–2.82 eV), 1.35–1.63 eV (2.31–2.41 eV), 1.56–2.10 eV (2.30–2.80 eV), and 1.19–1.74 eV (2.42–2.51 eV) for MoS_2 , MoSe_2 , WS_2 , and WSe_2 , respectively [55, 77, 78]. Given that the primary excitonic resonances of these materials typically lie within a narrow energy window of less than 200 meV, such deviations are unacceptably large for the reliable prediction of excitonic fingerprints. To mitigate

this issue, we place particular emphasis on achieving numerically converged results, employing fully relativistic, norm-conserving pseudopotentials that have been rigorously benchmarked. All calculations were subjected to thorough convergence testing to ensure the robustness of our predictions.

TABLE I. The calculated electronic properties of the considered materials. The presented values correspond to the direct band gap, indirect band-gap, K – Λ energy difference at lowest conduction levels, K – Γ energy difference at highest valence levels, and spin-orbit valence splitting at K/K', respectively, as defined in Figure 1. Here, the previously undefined acronyms refer to the following: LDA stands for Local Density Approximation, GGA for Generalized Gradient Approximation, and FP for Full Potential.

TMD	MTD	ΔE_{KK} (eV)	$\Delta E_{K\Lambda}$ (eV)	$\Delta E_{K\Gamma}^v$ (meV)	$\Delta E_{K\Lambda}^c$ (meV)	Δ_{SOC} (meV)	Ref
MoS ₂	PBE	1.566	1.859	11	-293	149	TW
	G ₀ W ₀	2.566	2.678	131	-113	149	TW
	PBE	1.690		20	-250		[5]
	G ₀ Mo ₀	2.750		160	-230		[5]
	LDA			145	-107		[79]
	FP	1.790		190	-50		[3]
	GGA	1.710		210		150	[6]
	FP			50		148	[4]
MoSe ₂	PBE	1.339	1.530	323	-191	185	TW
	G ₀ W ₀	2.269	2.374	306	-105	188	TW
	PBE	1.430		230	-230		[5]
	G ₀ W ₀	2.330		340	-330		[5]
	LDA			317	-171		[79]
	FP			360		183	[4]
WS ₂	PBE	1.537	1.665	212	-128	430	TW
	G ₀ W ₀	2.661	2.602	294	59	401	TW
	PBE	1.780		<2	-250		[5]
	G ₀ W ₀	2.880		60	-250		[5]
	LDA			237	-55		[79]
	FP			220		426	[4]
WSe ₂	PBE	1.198	1.352	430	-154	471	TW
	G ₀ W ₀	2.291	2.341	347	-50	442	TW
	PBE	1.500		260	-210		[5]
	G ₀ W ₀	2.380		340	-360		[5]
	LDA			484	-1		[79]
	FP			530		456	[4]

To further assess the accuracy of our computational framework, we compare our results with available experimental data. Angle-resolved photoemission spectroscopy (ARPES), in particular, provides high-resolution measurements of the highest occupied valence states and spin-orbit splittings. The experimentally reported values of $\Delta E_{K\Gamma}^v$, summarized in Table II, show considerable variability—even within similar sample types—likely arising from structural and environmental factors such as substrate-induced dielectric screening, residual strain, and variations in growth conditions. Despite these discrepancies, the consistent identification of the K point as the valence band maximum across all measurements reinforces the reliability of our theoretical predictions.

Moreover, our G₀W₀ calculations reproduce $\Delta E_{K\Gamma}^v$ val-

TABLE II. The experimental results for the band structure of the considered materials. Here, Ex, CVD, and MBE denote the growth techniques used to prepare the samples—Exfoliation, Chemical Vapor Deposition, and Molecular Beam Epitaxy, respectively. The quantities ΔE , SOC, X_B , $\Delta E_{K\Gamma}^v$, and T correspond to the estimated band gap, the spin-orbit-induced valence-band splitting at K/K', the binding energy of the direct exciton, the energy separation between the K and Γ points at the valence-band maximum, and the photoluminescence measurement temperature, respectively. SUB denotes the substrate.

TMD	EXP	SUB	ΔE (eV)	SOC (meV)	X_B (meV)	$\Delta E_{K\Gamma}^v$ (meV)	T (K)	REF
MoS ₂	Ex	<i>h</i> -BN	2.07	170		140	100	[10]
	CVD	Sp	2.11		240	20	300	[13]
	CVD	Au	1.90		90	60	300	[13]
	CVD	Gr				120	11	[27]
MoSe ₂	Ex	BN	1.64	220		480	100	[10]
	MBE	Gr	2.15	240		390	110	[14]
	Ex	Gr	2.18		550			[24]
	Ex	Gr		240		440	110	[12]
WS ₂	CVD	Gr	2.47	425		240	300	[22]
	Ex	BN	2.03	450		390	100	[10]
	CVD	Gr		440		200	8	[19]
	CVD	Gr	462			182	300	[20]
	CVD	TiO ₂		420		260	85	[23]
	CVD	Gr		420		200	300	[25]
	CVD	Si	2.04			150		[24]
	MBE	Gr	1.95	475	210	560	60	[9]
WSe ₂	MBE	Gr	2.12	440	500	640	77	[14]
	Ex	BN	1.79	485		620	100	[10]
	CVD	Sp	1.89		240	260	300	[13]
	CVD	Au	1.75		140	200	300	[13]
	Ex	Au		460		680	30	[11]
	Ex	Gr		490		500	110	[12]
	Ex	Si		513		892	300	[15]
	CVD	Gr		500		400	300	[16]

ues that are in close agreement with experimental results obtained from monolayers supported on graphene or encapsulated in hexagonal boron nitride (*h*-BN). The calculated spin-orbit splittings also show excellent agreement with experimental averages, with a slight systematic underestimation that remains within typical experimental uncertainty. In contrast, the G₀W₀ band gaps obtained in this study tend to exceed experimental values, which we attribute to extrinsic effects such as sample charging and band bending during optical or photoemission measurements, together with band gap reduction due to electron-phonon coupling. Nonetheless, the resulting direct exciton energies derived from our calculations are in very good agreement with experimental optical spectra, as discussed in the subsequent sections. Taken together, there is a robust correspondence between our highly converged G₀W₀ results and experimental benchmarks for $\Delta E_{K\Gamma}^v$ and spin-orbit splitting of monolayer TMDs.

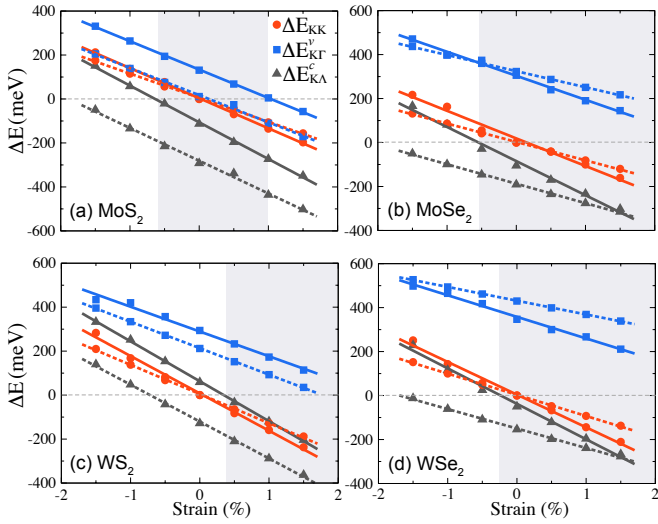


FIG. 2. Calculated PBE (dashed lines) and G_0W_0 (solid lines) band-gap transitions under biaxial strain for (a) MoS_2 , (b) MoSe_2 , (c) WS_2 , and (d) WSe_2 . The quantities Δ_{KK} , Δ_{KG} , and Δ_{KL} denote, respectively, the strain-induced change in the direct band gap at K (red circles), the energy difference between the highest valence states at K and Γ (blue squares), and the energy separation between the lowest conduction states at K and Λ (black triangles). The gray shaded area represents the strain windows where the band gap is direct at K.

2. Electronic properties: Strained

Strain engineering is already established as a powerful strategy for tailoring the electronic band structure of monolayer TMDs. Both theoretical and experimental studies have demonstrated that uniaxial or biaxial strain modulate the relative energies of conduction band valleys at the K, Λ , and Γ points, often inducing transitions between direct and indirect band gaps. First-principles and GW-BSE calculations show that tensile strain generally lowers the K-point conduction band edge while raising the Λ and Γ valleys, thereby increasing the energy separation between bright and momentum-forbidden excitonic states [79, 80]. This behaviour is clearly reflected in the strain-dependent quasiparticle band structures shown in Figs. S1–S4 of the Supplemental Materials (SM). These theoretical trends are consistent with experimental findings from photoluminescence and ARPES, which reveal redshifts in the direct gap and material-specific behaviour of dark valley states [81, 82]. Notably, recent strain-resolved PL measurements have introduced exciton strain gauge factors to quantify valley-specific responses, uncovering opposite strain-induced trends for K–K and K– Λ transitions in WSe_2 [53]. Collectively, these results underscore the versatility of strain as a tuning parameter for engineering valley-dependent electronic and excitonic properties in two-dimensional semiconductors.

Motivated by this, we performed a systematic investigation of the influence of biaxial strain on the electronic

properties, employing the same computational parameters used for the unstrained systems. Figure 2 presents both PBE and G_0W_0 results for the strain-induced evolution of the band structure, focusing on the variation of ΔE_{KG}^v and ΔE_{KL}^c across a biaxial strain range from -1.5% (compressive) to 1.5% (tensile). Changes in the direct bandgap at the K point, relative to its equilibrium value, are also shown, ΔE_{KK} . Notably, the slope of the strain-induced shifts in key energy levels—critical for determining excitonic behaviour—is strongly affected by many-body corrections, with particularly pronounced effects observed in Se-based compounds. This underscores the essential role of many-body interactions in accurately capturing the strain response of these materials as well.

The considerable changes in ΔE_{KG}^v and ΔE_{KL}^c with strain affects the intervalley ordering of zero-momentum (direct) and finite-momentum (indirect) excitonic states even at slight strain rates. For the G_0W_0 -corrected results, the calculated valence band maximum (VBM) remains at the K point within the strain range, except for MoS_2 , as indicated by the ΔE_{KG}^v values (blue curve in Fig. 2a). For MoS_2 , compressive strain beyond 1.0% (0.1%) shifts the VBM to the Γ point according to the G_0W_0 (PBE) results. Similar transitions occur at approximately 2.8% (4.4%), 2.6% (1.8%), and 3.6% (7.0%) strain for MoSe_2 , WS_2 , and WSe_2 , respectively. A similar analysis can be drawn from the ΔE_{KL}^c values, where negative values, coupled with positive ΔE_{KG}^v , are essential for a direct bandgap at the K point. The strain window that retains a direct bandgap, marked by shaded area in Figure 2, is notably narrower for S-based compounds, providing insights into potential bandgap engineering strategies. Considering G_0W_0 -corrected values and DFT errors in lattice constant predictions, determining the precise bandgap nature of these monolayers in their equilibrium state remains challenging. However, a direct bandgap is more likely for Se-based monolayers.

TABLE III. Exciton peak energy A (eV) and binding energy E_b (meV) for various 2D materials from this work and literature. Here, TW, WE, and GW refer to the calculations performed in this work, those obtained from the Wannier equation, and those computed using the GW-BSE method, respectively.

MoS_2		MoSe_2		WS_2		WSe_2		Method	Ref.
E_A	E_b	E_A	E_b	E_A	E_b	E_A	E_b		
1.94	625	1.70	570	2.08	580	1.75	530	TW	
1.97	850	1.66	750	2.17	710	1.75	670	GW	[43]
1.78	1030	1.50	910	1.84	1040	1.52	900	WE	[43]
1.87	1020	-	-	1.97	1050	-	-	GW	[44]
2.22	540			2.51	540			GW	[44]
2.04	630	-	-	-	-	-	-	GW	[46]
1.80	620							GW	[47]
1.98	-	-	-	-	-	1.65	-	TD-DFT	[48]
-	673		648		610		533	GW	[49]
-	-	1.62	510	-	-	-	-	GW	[45]
-	-	-	-	-	-	1.69	394	GW	[50]

3. Excitonic properties: Strain-free

As discussed above, many-body corrections significantly affect the key quasiparticle energy levels that govern the optical response of monolayer TMDs. To examine how these corrections influence excitonic features, we solved the Bethe–Salpeter equation on top of G_0W_0 quasiparticle energies using the Yambo code. The lowest-energy bright exciton in all four materials is governed predominantly by electron–hole interactions at the K point, labeled as DX_{KK} in Fig. 1(a). This state, denoted as the A-exciton in the literature, exhibits excitation energies of 1.94, 1.70, 2.08, and 1.75 eV for monolayer MoS_2 , $MoSe_2$, WS_2 , and WSe_2 , respectively. These values show excellent agreement with low-temperature photoluminescence measurements, which report A-exciton peaks in the ranges of 1.90–1.95 eV for MoS_2 [28, 29, 34–36], 1.64–1.66 eV for $MoSe_2$ [29–33, 83, 84], 2.08–2.12 eV for WS_2 [51, 53, 54, 85, 86], and 1.72–1.75 eV for WSe_2 [29, 52, 53, 56, 83, 87–92]. This close correspondence underscores the predictive accuracy of our G_0W_0 +BSE approach for capturing the fundamental excitonic properties of these monolayers. These results are summarized in Table III, along with previously published GW-BSE values. The corresponding A-exciton energies obtained in our calculations fall within the spread of earlier theoretical reports: 1.78–2.22 eV for MoS_2 , 1.50–1.66 eV for $MoSe_2$, 1.84–2.51 eV for WS_2 , and 1.52–1.75 eV for WSe_2 .

Furthermore, our calculations accurately reproduce the A–B exciton energy splitting arising from spin–orbit coupling in the valence band. We obtain splittings of 144, 195, and 358 meV for MoS_2 , $MoSe_2$, and WS_2 , respectively, which compare favourably with the experimentally reported values of approximately 150 meV [28, 36, 93], 200 meV, and 380 meV [86, 93].

Exciton binding energies (E_b) reported in the literature span a broad range, largely due to variations in sample quality, measurement techniques, and environmental screening. For example, experimental E_b values for A-exciton range from 217 to 640 meV for monolayer MoS_2 [37, 42, 94–97], 216 to 590 meV for $MoSe_2$ [14, 24, 37, 42, 83, 94], 174 to 700 meV for WS_2 [37, 42, 93, 94, 96], 167 to 720 meV for WSe_2 [37, 42, 92, 94, 95]. Our G_0W_0 -BSE calculations yield the A binding energies of 625 meV (MoS_2), 570 meV ($MoSe_2$), 580 meV (WS_2), and 530 meV (WSe_2), placing them toward the upper bounds of the experimental ranges. Some early theoretical works report binding energies exceeding 1 eV [43, 44], but these values often originate from simplified analytical models—such as Mott–Wannier model excitons—combined with GW-derived quasiparticle gaps, rather than full GW-BSE calculations. When the same studies employ a proper ab initio GW-BSE approach, the resulting binding energies align more closely with ours, emphasizing the critical role of explicitly treating the electron–hole interaction [43].

In addition to excitonic states with zero center-of-mass

TABLE IV. Unstrained exciton energies (in eV) for various monolayer TMDs from this work and prior literature datasets. Here, TW, WE, and GW refer to the calculations performed in this work, those obtained from the Wannier model equation, and those computed using the GW-BSE method, respectively.

TMD	DX_{KK}	$IDX_{\Gamma K}$	$IDX_{K\Lambda}$	$IDX_{\Gamma\Lambda}$	$IDX_{K'\Lambda}$	MTD	REF
MoS_2	1.94	1.96	2.01	2.03	2.00	TW	
	1.84	1.91	1.90	-	-	WE	[79]
	2.16	-	2.18	-	-	GW	[98]
$MoSe_2$	1.71	1.90	1.78	2.00	1.76	TW	
	1.51	1.73	1.65	-	-	WE	[79]
	1.80	-	1.83	-	-	GW	[98]
WS_2	2.08	2.22	1.96	2.11	1.94	TW	
	2.08	-	1.91	-	-	EXP	[99]
	2.08	2.27	2.04	2.16	-	WE	[53]
	1.99	2.14	1.98	-	-	WE	[79]
	2.00	2.20	1.97	-	-	WE	[80]
WSe_2	2.17	-	2.11	-	-	GW	[98]
	1.76	1.96	1.76	2.01	1.74	TW	
	1.67	-	1.70	-	-	EXP	[82]
	1.74	2.17	1.69	2.02	-	WE	[53]
	1.65	2.05	1.59	-	-	WE	[79]
	1.78	-	1.72	-	-	GW	[98]

momentum, we investigated finite-momentum excitons with $\mathbf{Q} = \Lambda$, K, and M. For each momentum transfer, we analyzed the k -resolved exciton weights (as defined in the Section II) and identified the lowest-energy excitonic states with dominant contributions corresponding to the $K \iff \Lambda$ (with momentum Λ), $\Gamma \iff \Lambda$ (with momentum Λ), $\Gamma \iff K$ (with momentum K), and $K' \iff \Lambda$ (with momentum M) transitions, as schematically illustrated in Fig. 1. The calculated energies for these indirect excitons (IDXs), labeled as $IDX_{K\Lambda}$, $IDX_{\Gamma\Lambda}$, $IDX_{\Gamma K}$, and $IDX_{K'\Lambda}$, are presented in Table IV. The full k -space dispersion of these states—highlighting their characteristic multivalley structure—are provided in Fig. S5 of the Supplemental Material.

To the best of our knowledge, only one experimental study has reported finite-momentum excitons for both WS_2 and WSe_2 [82, 99] monolayers. For WS_2 , our results show good agreement, with an exact match for the direct exciton and a deviation of only \sim 50 meV for $IDX_{K\Lambda}$. For WSe_2 , our calculations of 90 meV and 60 meV overestimate the DX_{KK} and $IDX_{K\Lambda}$. Although not in perfect quantitative agreement, these discrepancies remain within typical experimental uncertainties. Furthermore, the DFT-relaxed structures may not fully reproduce the actual crystal configurations in experimental samples, and even small structural variations can produce noticeable shifts in excitonic energies. These factors, discussed further in the following section, likely account for the residual differences.

Several theoretical values for excitonic energies have been reported, obtained either by solving the Wannier equation with a generalized Rytova–Keldysh screened Coulomb potential using strain-adapted band parame-

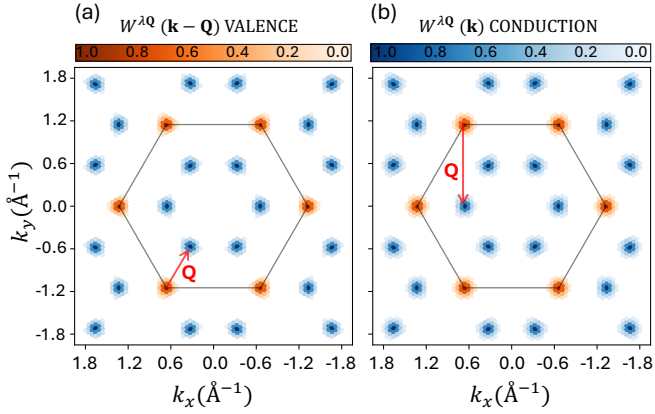


FIG. 3. Calculated excitonic weights of MoS₂ for (a) IDX_{KΛ} and (b) IDX_{K'Λ} (see Table III), summed over all bands across the Brillouin zone (Eq. (4)) and shown for every equivalent \mathbf{Q} -vector. The colour scales highlight the regions corresponding to the dominant electron-hole transitions for each chosen excitonic state and momentum.

ters from DFT calculations [53, 79, 80], or within the GW+BSE framework [98]. When compared with these studies, as well as with the results obtained in the present work, clear deviations exist in the excitonic fingerprints—namely, the absolute energies of direct and indirect excitons and their relative energy separation, as seen in Table IV. For the DFT band-structure-based analyses, these discrepancies most likely arise from the fact noted above: many-body corrections not only shift the absolute band gap but also modify the relative energy differences between the conduction- and valence-band valleys, which in turn directly influence the excitonic fingerprints.

For the indirect excitons, we further note the small energy difference between the IDX_{KΛ} and IDX_{K'Λ} states (10-20 meV), which both involve transitions between the same bands, yet with different momentum. To clarify this behaviour, for the IDX_{KΛ} and IDX_{K'Λ} excitons of MoS₂, we analyzed the excitonic weights, which quantify the dominant valence $|A_{cv}^λ(\mathbf{k} - \mathbf{Q})|^2$ and conduction $|A_{cv}^λ(\mathbf{k})|^2$ band contributions to each excitonic state (see Eq. 4). As shown in Fig. 3(a) and (b), both excitons, although located at different transfer momenta, are composed of the same electron and hole states. This strong similarity in their underlying band-structure contributions naturally explains the small energy splitting observed between the IDX_{KΛ} and IDX_{K'Λ} excitons, which is then entirely determined by the \mathbf{Q} -dependence of the electron-hole interaction kernel $\Xi(\mathbf{Q})$ (see Eq. (2)). However, despite their similar electronic character, the temperature-dependent population and excitation dynamics of these intervalley excitons will differ significantly, both because their energy separation corresponds to an effective temperature difference of 100-200 K, and because phonon-mediated scattering rates for these indirect states will depend on lattice vibrations with different energies and momenta.

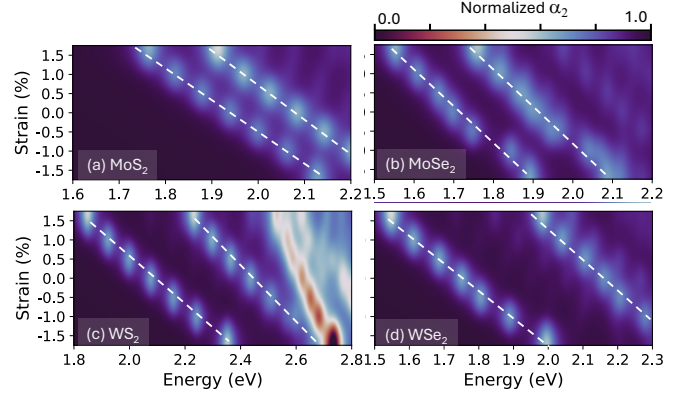


FIG. 4. Strain dependence of the direct exciton energies for (a) MoS₂, (b) MoSe₂, (c) WS₂, and (d) WSe₂. The colourmap indicates the evolution of the normalized 2D polarizability α_2 . The ground-state A and B excitonic transitions are highlighted, with white dashed lines denoting bright states and gray dashed lines marking dark spin-triplet states.

4. Excitonic properties: Strained

Building on the growing interest in strain engineering as an effective strategy to modulate excitonic properties in transition metal dichalcogenides, we present a systematic investigation of the strain dependence of exciton energies in MoS₂, MoSe₂, WS₂, and WSe₂. While previous studies have offered valuable insights into the strain response of individual excitonic states, our results provide a comprehensive comparative picture of strain-exciton coupling in the monolayer TMD materials family.

The colour maps in Fig. 4 (a), (b), (c), and (d) display the evolution of the optical absorption spectra represented by the imaginary part of 2D polarizability, α_2 from Eq. (6), for monolayer MoS₂, MoSe₂, WS₂, and WSe₂, respectively. The dashed white lines trace the strain-induced shifts of the peak positions of the spin-orbit-split bright direct excitons, labeled A and B, corresponding to the DX_{KK} states. In addition, there are also the spin-triplet dark states (also observed experimentally[100]), which lie energetically below the bright singlet states. With respect to the A-exciton energies, they are predicted to lie 16, 1, 40, and 24 meV below for MoS₂, MoSe₂, WS₂, and WSe₂, respectively. These dark states are in quantitative agreement with literature[50, 74, 101] and follow the same strain-induced trends as the bright excitons.

To quantitatively assess strain sensitivity, we evaluate the excitonic strain gauge factor—commonly employed in experimental characterization-, $\Omega = dE_X/d\varepsilon$, where E_X is the corresponding strain dependent exciton energy and ε is the strain (expressed in meV / strain percentage). The resulting values for A and B exciton are summarized in Table V. The values for A-exciton are systematically larger than those obtained from the Wannier equation using DFT-derived effective masses and band edges [79]. However, for W-based compounds, calculations based on

TABLE V. Strain gauge factors (in meV/%) for direct (DX_{KK}) and indirect ($IDX_{K\Gamma}$, $IDX_{K\Lambda}$) excitons in strained monolayer TMDs. Here, TW, WE, and EXP refer to the calculations performed in this work, those obtained from the Wannier equation, and those measured experimentally, respectively.

TMD	A	B	$IDX_{K\Gamma}$	$IDX_{K\Lambda}$	$IDX_{\Gamma\Lambda}$	$IDX_{K'\Lambda}$	$IDX_{KK'}$	MTD	Ref.
MoS ₂	-121	-118	-233	37	-81	36	-120	TW	
	-72	-	-142	10.1	-	-	-	WE	[79]
MoSe ₂	-112	-111	-201	34	-75	35	-111	TW	
	-65	-	-123	8	-	-	-	WE	[79]
WS ₂	-164	-160	-261	27	-90	28	-156	TW	
	-102	-	-	-	-68	-	-	EXP	[53]
	-60	-	-123	37	-	-	-	WE	[79]
	-113	-	-236	74	-	-	-	WE	[80]
WSe ₂	-125	-	-223	45	-52	-	-	WE	[53]
	-143	-122	-228	18	-73	18	-139	TW	
	-46	-	-	22	-	-	-	EXP	[82]
	-118	-	-	34	-	-	-	EXP	[53]
WSe ₂	-54	-	-106	37	-	-	-	WE	[79]
	-111	-	-197	43	-51	-	-	WE	[53]

a similar Wannier–Keldysh approach [53] yield results that are comparable with ours. The pronounced redshift in the energy of the A-exciton under applied tensile strain, as predicted for all the considered monolayers, is consistent with photoluminescence (PL) measurements [53, 81]. The experimental strain gauge factors for A-exciton shifts are reported as -102 meV/% for WS₂ and -118 meV/% and -46 meV/% for WSe₂. Our calculations yield -164 meV/% for WS₂ and -143 meV/% for WSe₂, systematically exceeding the experimental values. Given the lack of a direct one-to-one correspondence between theory and experiment regarding the actual strain applied to the samples, this discrepancy does not indicate a significant error.

To elucidate more the origin of these shifts, we compare them with the strain-induced variations of the direct band gap at the K point, obtained from G_0W_0 -corrected band-gap values (Fig. 2). The calculated gauge factors for the direct exciton energy and the corresponding band gap gauge factors depicted in Table VI are close to each other, indicating that the change in band gap is the primary driver of the direct exciton redshift under strain.

To gain insight into the strain response of the indirect

TABLE VI. Calculated strain gauge factors (in meV/%) for the band gaps (ΔE) associated with direct and indirect exciton formation.

Material	ΔE_{KK}	$\Delta E_{K\Gamma}$	$\Delta E_{K\Lambda}$	$\Delta E_{\Gamma\Lambda}$	Calc.
MoS ₂	-137	-266	30	-99	G_0W_0
	-109	-233	39	-84	PBE
MoSe ₂	-126	-235	29	-80	G_0W_0
	-84	-157	5	-69	PBE
WS ₂	-170	-283	12	-101	G_0W_0
	-133	-253	35	-85	PBE
WSe ₂	-149	-248	13	-86	G_0W_0
	-96	-159	-8	-71	PBE

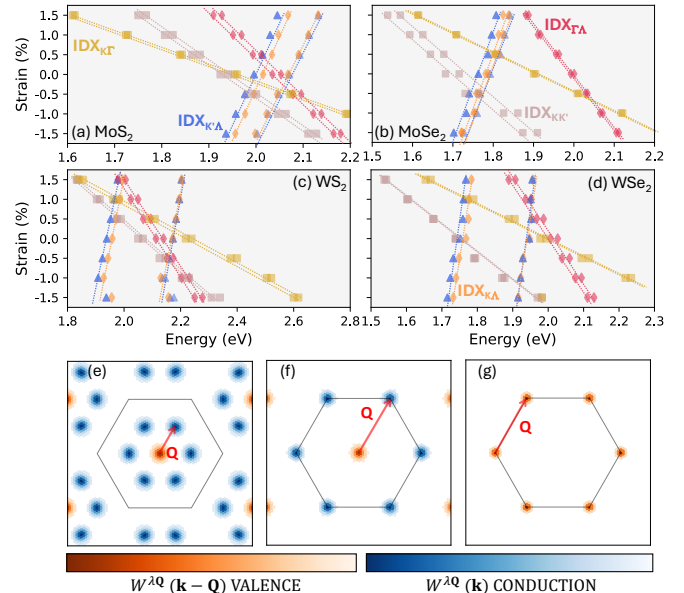


FIG. 5. Strain dependence of the energies of the indirect excitons, $IDX_{K'\Lambda}$ (blue triangles), $IDX_{K\Lambda}$ (orange diamonds), $IDX_{\Gamma\Lambda}$ (red diamonds), $IDX_{\Gamma K}$ (yellow squares), and $IDX_{KK'}$ (pink squares), for (a) MoS₂, (b) MoSe₂, (c) WS₂, and (d) WSe₂. The corresponding excitonic weight distributions for (e) $DX_{\Gamma\Lambda}$, (f) $IDX_{\Gamma K}$, and (g) $IDX_{KK'}$ are also shown, similarly to Fig. 3. The colour maps represent the normalized weights on a linear scale.

excitonic manifold, we analyze the structure of the excitonic wave functions, by examining the lowest-energy indirect excitons corresponding to the most important valleys, as discussed above, also including the higher energy states for each valley: in particular, we analyze the first ten states for $IDX(\mathbf{Q} = \Lambda)$, $IDX(\mathbf{Q} = K)$, and $IDX(\mathbf{Q} = M)$, as shown in Figs. S6-S10 in SM.

The linear blue shift of the $IDX(\mathbf{Q} = M)$ excitons is consistently observed across all considered materials, indicating that excitons within the examined energy window possess nearly identical gauge factors. To further substantiate this behaviour, we focus on the strain evolution of the ground-state (degenerate) exciton and the next excited state, highlighted by blue triangles in Figs. 5(a-d). These excitons exhibit the characteristic $IDX_{K'\Lambda}$ weight distribution shown in Fig. 3(b), with only minor strain-induced modifications. As expected for excitons dominated by a single valley pair, their strain dependence closely follows the evolution of the underlying indirect conduction–valence band gap, as presented in Fig. S10 of the Supplemental Material.

In the unstrained case, these $IDX_{K'\Lambda}$ excitons lie at higher energies than the direct DX_{KK} exciton in Mo-based systems, whereas they appear at lower energies in W-based systems. However, owing to the opposite strain response of these indirect excitonic states compared to direct excitons, several $IDX_{K'\Lambda}$ excitons become energetically favourable and fall well below the A-exciton for all

materials already at a compressive strain of 1.5%.

The $\text{ID}(\mathbf{Q} = \Lambda)$ excitons, indicated by red diamonds in Figs. 5(a-d), exhibit a more intricate strain response. Unlike excitons at other center-of-mass momenta, two distinct groups with opposite strain dependencies are clearly resolved, particularly in MoS_2 and WS_2 . A systematic analysis of the excitonic weight distributions elucidates the microscopic origin of this behaviour. Specifically, two different types of electronic transitions to the conduction Λ valley, either from Γ or from K in valence, contribute to the low-energy $\mathbf{Q} = \Lambda$ excitonic valley. At higher energies, this gives rise to hybridized states with a broad momentum distribution that is not strongly localized around the Γ , Λ or K points. To avoid ambiguities arising from such hybridization, we focus on the lowest-energy exciton each type, which is strongly localized: the $\text{IDX}_{K\Lambda}$ exciton weight distribution was already presented in Fig. 3(a), while the $\text{IDX}_{\Gamma\Lambda}$ states are shown in Fig. 5(e).

The predicted opposite intravalley gauge factors for $\text{IDX}_{\Gamma\Lambda}$ and $\text{IDX}_{K\Lambda}$ are consistent with the corresponding strain-dependent band-gap trends shown in Fig. S10. Moreover, the nearly identical gauge factors obtained for $\text{IDX}_{K\Lambda}$ and $\text{IDX}_{K'\Lambda}$ are naturally explained by the fact that their underlying band-gap trend is the same. Our calculations further demonstrate that $\text{IDX}_{\Gamma\Lambda}$ excitons always remain at higher energies than the direct DX_{KK} exciton, whereas $\text{IDX}_{K\Lambda}$, analogous to $\text{IDX}_{K'\Lambda}$, becomes a well-separated low-energy state under compressive strain.

For $\text{IDX}(\mathbf{Q} = K)$ excitons, a clear linear strain dependence is observed, most prominently in WSe_2 (and similarly in WS_2 and MoSe_2). However, analogous to the $\mathbf{Q} = \Lambda$ case, band and valley hybridization complicate a unique assignment of excitonic character across the full strain range. We therefore focus on the two most localized low-energy excitonic transitions, namely the $K-K'$ and $\Gamma-K$ configurations, denoted as $\text{IDX}_{KK'}$ and $\text{IDX}_{\Gamma K}$, respectively, as illustrated in Figs. 5(f) and 5(g).

The strain dependence of $\text{IDX}_{KK'}$ (rose squares) closely mirrors that of the direct DX_{KK} exciton, as expected since they originate from the same electron-hole wavefunctions and from their nearly identical k -space weight distributions. In contrast, the $K-\Gamma$ localized exciton $\text{IDX}_{\Gamma K}$ (yellow squares) exhibits a noticeably larger redshift gauge factor and becomes energetically lower than the A -exciton in MoS_2 and WS_2 already at 1.5% tensile strain.

The strain gauge factors extracted for the identified excitons are summarized in Table V. Overall, the qualitative trends are consistent with those obtained from Wannier-Keldysh approaches, although noticeable quantitative deviations remain. In particular, the values reported by Khatibi *et al.* differ substantially from our predictions, whereas the gauge factors computed by Kumar *et al.* for $\text{IDX}_{K\Gamma}$ are in close agreement with our results. For the $\text{IDX}_{\Gamma\Lambda}$ exciton, Kumar *et al.* [53] experimentally reported a gauge factor of $-68 \text{ meV}/\%$ in monolayer WS_2 , and a positive gauge factor of $+34 \text{ meV}/\%$ for $\text{IDX}_{K\Lambda}$ in WSe_2 , opposite in sign to $\text{IDX}_{\Gamma\Lambda}$ in WS_2 . In our

calculations, these values are obtained as -90 and $+18 \text{ meV}/\%$, respectively, reproducing the experimentally observed qualitative behaviour. For $\text{IDX}_{K\Lambda}$ in WSe_2 , Aslan *et al.* [82] likewise confirmed a positive gauge factor of $+22 \text{ meV}/\%$, again consistent with our findings. We note, however, that the same study reported a DX_{KK} gauge factor that differs significantly from both our results and those of Kumar *et al.* The opposite strain responses of $\text{IDX}_{\Gamma\Lambda}$ and $\text{IDX}_{K\Lambda}$ were further corroborated by Wannier-Keldysh calculations in Ref. [53], yielding -52 and $+45 \text{ meV}/\%$ for WS_2 and -51 and $+43 \text{ meV}/\%$ for WSe_2 , respectively. In summary, while full quantitative agreement with the experimental literature has not yet been achieved, our results capture the correct qualitative behaviour and provide a more detailed microscopic understanding of the origin of these strain-induced exciton shifts.

Going back to the level of single-particle band structure, we computed the indirect band-gap shifts, as previously done for the direct case, by identifying the valence and conduction band edges that correspond to the main exciton valleys (Table VI). As already remarked, the resulting G_0W_0 gauge factors show clear correspondence with those extracted for the associated excitons. Furthermore, the opposite strain responses of $\text{IDX}_{\Gamma\Lambda}$ and $\text{IDX}_{K\Lambda}$, also observed experimentally, closely follows the behaviour of their respective band edges, reinforcing the direct link between valley-specific band-structure modifications and excitonic shifts. The discrepancies between the gauge factors obtained at the G_0W_0 and PBE levels are substantial. Given the near one-to-one correspondence between band-edge shifts and exciton energies, these differences underscore the necessity of many-body-corrected band structures when modeling strain responses within simplified excitonic frameworks. Indeed, even small energy variations in the excitonic picture can significantly affect the interpretation of experimental observations.

III. CONCLUSION

The combined analysis of experimental ARPES, photoluminescence measurements, and strain-dependent gauge factors, together with highly accurate many-body calculations of both direct and indirect excitons in MoS_2 , MoSe_2 , WS_2 , and WSe_2 , provides a detailed and coherent picture of the landscape of low-energy electronic excitations in these materials. In particular, the strain-dependent results reveal the critical role of valley-specific band-structure modifications in governing the energetic ordering, hybridization, and momentum-space character of excitonic states. This comprehensive comparison establishes a consistent physical interpretation of the exciton behaviour across the TMD family and underscores the importance of strain as a key tuning parameter for exciton engineering in two-dimensional semiconductors.

Most importantly, the landscape of low-lying indi-

rect exciton states exhibits significant intervalley and intravalley overlap in an energy window of a few hundred meV. Because strain strongly modifies the relative energies of the conduction-band minima at K and Λ and the valence-band maxima at K and Γ , the degree of hybridization and even the energetic ordering of these indirect excitons undergo significant strain-dependent rearrangements. This sensitivity provides direct insight into the microscopic origin of strain-driven excitonic shifts and highlights the need for many-body-corrected band structures when interpreting or predicting strain responses in TMD monolayers, as well as for calculations of binding energies, effective masses, and magnetic *g*-factors.

These findings also clarify the limitations of simplified two-particles or effective-mass descriptions for excitons in transition-metal dichalcogenide monolayers. While such models can capture qualitative trends for direct excitons due to localized electronic transitions at band valley extrema, it is much more difficult to account for indirect excitons due to competing intervalley transitions, for non-parabolicities in the band dispersions, and for the many-body effects that govern the low-lying indirect exciton manifold. For example, the different distributions of excitonic weights across the K, K', Λ , and Γ valleys, to-

gether with their pronounced and varied strain dependence, highlight how accurate many-body calculations can provide a valuable foundation for characterising and modeling excitonic properties. Indeed, reliable computational results for excited-state energies and wavefunctions can be used as inputs or fitting parameters for simplified models aiming to describe more complicated phenomena involving low-energy electronic excitations, such as nonequilibrium spectroscopies, dynamics, transport and condensation. This would combine the computational efficiency and versatility of effective descriptions with the quantitative accuracy of many-body first-principles simulations.

ACKNOWLEDGEMENTS

This work was supported by the Research Foundation-Flanders (FWO) and the Special Research Funds of the University of Antwerp (BOF-UA). F.P. acknowledges funding by ICSC - Centro Nazionale di Ricerca in High Performance Computing, Big Data and Quantum Computing – funded by the European Union through the Italian Ministry of University and Research under PNRR M4C2I1.4 (Grant No. CN00000013).

- [1] Y. Liu, X. Duan, H.-J. Shin, S. Park, Y. Huang, and X. Duan, Promises and prospects of two-dimensional transistors, *Nature* **591**, 43–53 (2021).
- [2] S. Das, A. Sebastian, E. Pop, C. J. McClellan, A. D. Franklin, T. Grasser, T. Knobloch, Y. Illarionov, A. V. Penumatcha, J. Appenzeller, Z. Chen, W. Zhu, I. Asselberghs, L.-J. Li, U. E. Avci, N. Bhat, T. D. Anthopoulos, and R. Singh, Transistors based on two-dimensional materials for future integrated circuits, *Nature Electronics* **4**, 786–799 (2021).
- [3] E. S. Kadantsev and P. Hawrylak, Electronic structure of a single mos₂ monolayer, *Solid state communications* **152**, 909 (2012).
- [4] Z. Y. Zhu, Y. C. Cheng, and U. Schwingenschlögl, Giant spin-orbit-induced spin splitting in two-dimensional transition-metal dichalcogenide semiconductors, *Physical Review B—Condensed Matter and Materials Physics* **84**, 153402 (2011).
- [5] Y. Liang, S. Huang, R. Soklaski, and L. Yang, Quasiparticle band-edge energy and band offsets of monolayer of molybdenum and tungsten chalcogenides, *Applied physics letters* **103** (2013).
- [6] O. V. Yazyev and A. Kis, Mos₂ and semiconductors in the flatland, *Materials Today* **18**, 20 (2015).
- [7] K. F. Mak, C. Lee, J. Hone, J. Shan, and T. F. Heinz, Atomically thin mos₂: A new direct-gap semiconductor, *Physical Review Letters* **105**, 10.1103/physrevlett.105.136805 (2010).
- [8] D. Xiao, G.-B. Liu, W. Feng, X. Xu, and W. Yao, Coupled spin and valley physics in monolayers of mos₂ and other group-vi dichalcogenides, *Phys. Rev. Lett.* **108**, 196802 (2012).
- [9] Y. Zhang, M. M. Ugeda, C. Jin, S.-F. Shi, A. J. Bradley, A. Martín-Recio, H. Ryu, J. Kim, S. Tang, Y. Kim, *et al.*, Electronic structure, surface doping, and optical response in epitaxial wse₂ thin films, *Nano letters* **16**, 2485 (2016).
- [10] P. V. Nguyen, N. C. Teutsch, N. P. Wilson, J. Kahn, X. Xia, A. J. Graham, V. Kandyba, A. Giampietri, A. Barinov, G. C. Constantinescu, *et al.*, Visualizing electrostatic gating effects in two-dimensional heterostructures, *Nature* **572**, 220 (2019).
- [11] W. Zhao, Y. Huang, C. Shen, C. Li, Y. Cai, Y. Xu, H. Rong, Q. Gao, Y. Wang, L. Zhao, *et al.*, Electronic structure of exfoliated millimeter-sized monolayer wse₂ on silicon wafer, *Nano Research* **12**, 3095 (2019).
- [12] N. R. Wilson, P. V. Nguyen, K. Seyler, P. Rivera, A. J. Marsden, Z. P. Laker, G. C. Constantinescu, V. Kandyba, A. Barinov, N. D. Hine, *et al.*, Determination of band offsets, hybridization, and exciton binding in 2d semiconductor heterostructures, *Science advances* **3**, e1601832 (2017).
- [13] S. Park, N. Mutz, T. Schultz, S. Blumstengel, A. Han, A. Aljarb, L.-J. Li, E. J. List-Kratochvil, P. Amsalem, and N. Koch, Direct determination of monolayer mos₂ and wse₂ exciton binding energies on insulating and metallic substrates, *2D Materials* **5**, 025003 (2018).
- [14] C. Zhang, Y. Chen, A. Johnson, M.-Y. Li, L.-J. Li, P. C. Mende, R. M. Feenstra, and C.-K. Shih, Probing critical point energies of transition metal dichalcogenides: surprising indirect gap of single layer wse₂, *Nano letters* **15**, 6494 (2015).
- [15] D. Le, A. Barinov, E. Preciado, M. Isarraraz, I. Tanabe, T. Komesu, C. Troha, L. Bartels, T. S. Rahman, and

P. A. Dowben, Spin-orbit coupling in the band structure of monolayer wse₂, *Journal of Physics: Condensed Matter* **27**, 182201 (2015).

[16] S. Agnoli, A. Ambrosetti, T. O. Mentes, A. Sala, A. Locatelli, P. L. Silvestrelli, M. Cattelan, S. Eichfeld, D. D. Deng, J. A. Robinson, *et al.*, Unraveling the structural and electronic properties at the wse₂-graphene interface for a rational design of van der waals heterostructures, *ACS Applied Nano Materials* **1**, 1131 (2018).

[17] S. Ulstrup, Y. in't Veld, J. A. Miwa, A. J. Jones, K. M. McCreary, J. T. Robinson, B. T. Jonker, S. Singh, R. J. Koch, E. Rotenberg, *et al.*, Observation of interlayer plasmon polaron in graphene/ws₂ heterostructures, *Nature Communications* **15**, 3845 (2024).

[18] F. Bussolotti, J. Yang, H. Kawai, J. Y. Chee, and K. E. J. Goh, Influence of many-body effects on hole quasiparticle dynamics in a ws₂ monolayer, *Physical Review B* **103**, 045412 (2021).

[19] H. Henck, Z. Ben Aziza, D. Pierucci, F. Laourine, F. Reale, P. Palczynski, J. Chaste, M. G. Silly, F. Bertran, P. Le Fevre, *et al.*, Electronic band structure of two-dimensional ws₂/graphene van der waals heterostructures, *Physical Review B* **97**, 155421 (2018).

[20] S. Forti, A. Rossi, H. Büch, T. Cavallucci, F. Bisio, A. Sala, T. O. Mentes, A. Locatelli, M. Magnozzi, M. Canepa, *et al.*, Electronic properties of single-layer tungsten disulfide on epitaxial graphene on silicon carbide, *Nanoscale* **9**, 16412 (2017).

[21] J. Katoch, S. Ulstrup, R. J. Koch, S. Moser, K. M. McCreary, S. Singh, J. Xu, B. T. Jonker, R. K. Kawakami, A. Bostwick, *et al.*, Giant spin-splitting and gap renormalization driven by trions in single-layer ws₂/h-bn heterostructures, *Nature Physics* **14**, 355 (2018).

[22] C. Kastl, C. Chen, R. Koch, B. Schuler, T. Kuykendall, A. Bostwick, C. Jozwiak, T. Seyller, E. Rotenberg, A. Weber-Bargioni, *et al.*, Multimodal spectromicroscopy of monolayer ws₂ enabled by ultra-clean van der waals epitaxy, *2D Materials* **5**, 045010 (2018).

[23] S. Ulstrup, J. Katoch, R. J. Koch, D. Schwarz, S. Singh, K. M. McCreary, H. K. Yoo, J. Xu, B. T. Jonker, R. K. Kawakami, *et al.*, Spatially resolved electronic properties of single-layer ws₂ on transition metal oxides, *ACS nano* **10**, 10058 (2016).

[24] M. M. Ugeda, A. J. Bradley, S.-F. Shi, F. H. Da Jornada, Y. Zhang, D. Y. Qiu, W. Ruan, S.-K. Mo, Z. Hussain, Z.-X. Shen, *et al.*, Giant bandgap renormalization and excitonic effects in a monolayer transition metal dichalcogenide semiconductor, *Nature materials* **13**, 1091 (2014).

[25] J. Zribi, D. Pierucci, F. Bisti, B. Zheng, J. Avila, L. Khalil, C. Ernandes, J. Chaste, F. Oehler, M. Pala, *et al.*, Unidirectional rashba spin splitting in single layer ws₂ (1-x) se₂x alloy, *Nanotechnology* **34**, 075705 (2022).

[26] S.-K. Mo, C. Hwang, Y. Zhang, M. Fanciulli, S. Muff, J. H. Dil, Z.-X. Shen, and Z. Hussain, Spin-resolved photoemission study of epitaxially grown mose₂ and wse₂ thin films, *Journal of physics: Condensed matter* **28**, 454001 (2016).

[27] F. Bussolotti, H. Kawai, S. L. Wong, and K. E. J. Goh, Protected hole valley states in single-layer mo s₂, *Physical Review B* **99**, 045134 (2019).

[28] M. Tangi, M. K. Shakfa, P. Mishra, M.-Y. Li, M.-H. Chiu, T. K. Ng, L.-J. Li, and B. S. Ooi, Anomalous photoluminescence thermal quenching of sandwiched single layer mos₂, *Optical Materials Express* **7**, 3697 (2017).

[29] S. Tongay, J. Suh, C. Ataca, W. Fan, A. Luce, J. S. Kang, J. Liu, C. Ko, R. Raghunathanan, J. Zhou, *et al.*, Defects activated photoluminescence in two-dimensional semiconductors: interplay between bound, charged and free excitons, *Scientific reports* **3**, 2657 (2013).

[30] J. S. Ross, S. Wu, H. Yu, N. J. Ghimire, A. M. Jones, G. Aivazian, J. Yan, D. G. Mandrus, D. Xiao, W. Yao, *et al.*, Electrical control of neutral and charged excitons in a monolayer semiconductor, *Nature communications* **4**, 1474 (2013).

[31] A. Arora, K. Nogajewski, M. Molas, M. Koperski, and M. Potemski, Exciton band structure in layered mose₂: from a monolayer to the bulk limit, *Nanoscale* **7**, 20769 (2015).

[32] X. Lu, M. I. B. Utama, J. Lin, X. Gong, J. Zhang, Y. Zhao, S. T. Pantelides, J. Wang, Z. Dong, Z. Liu, *et al.*, Large-area synthesis of monolayer and few-layer mose₂ films on sio₂ substrates, *Nano letters* **14**, 2419 (2014).

[33] T. Hotta, S. Higuchi, A. Ueda, K. Shinokita, Y. Miyauchi, K. Matsuda, K. Ueno, T. Taniguchi, K. Watanabe, and R. Kitaura, Exciton diffusion in h bn-encapsulated monolayer mo se₂, *Physical Review B* **102**, 115424 (2020).

[34] D. Vaquero, V. Clericò, J. Salvador-Sánchez, A. Martín-Ramos, E. Díaz, F. Domínguez-Adame, Y. M. Meziani, E. Diez, and J. Quereda, Excitons, trions and rydberg states in monolayer mos₂ revealed by low-temperature photocurrent spectroscopy, *Communications Physics* **3**, 194 (2020).

[35] D. Li, Z. Xiao, H. R. Golgir, L. Jiang, V. R. Singh, K. Keramatnejad, K. E. Smith, X. Hong, L. Jiang, J.-F. Silvain, *et al.*, Large-area 2d/3d mos₂-moo₂ heterostructures with thermally stable exciton and intriguing electrical transport behaviors, *Advanced Electronic Materials* **3**, 1600335 (2017).

[36] J. W. Christopher, B. B. Goldberg, and A. K. Swan, Long tailed trions in monolayer mos₂: Temperature dependent asymmetry and resulting red-shift of trion photoluminescence spectra, *Scientific reports* **7**, 14062 (2017).

[37] M. Goryca, J. Li, A. V. Stier, T. Taniguchi, K. Watanabe, E. Courtade, S. Shree, C. Robert, B. Urbaszek, X. Marie, and S. A. Crooker, Revealing exciton masses and dielectric properties of monolayer semiconductors with high magnetic fields, *Nature Communications* **10**, 10.1038/s41467-019-12180-y (2019).

[38] M. Turunen, M. Brotons-Gisbert, Y. Dai, Y. Wang, E. Scerri, C. Bonato, K. D. Jöns, Z. Sun, and B. D. Gerardot, Quantum photonics with layered 2d materials, *Nature Reviews Physics* **4**, 219–236 (2022).

[39] M. Esmann, S. C. Wein, and C. Antón-Solanas, Solid-state single-photon sources: Recent advances for novel quantum materials, *Advanced Functional Materials* **34**, 10.1002/adfm.202315936 (2024).

[40] W. Yang, J. Shang, J. Wang, X. Shen, B. Cao, N. Peimyoo, C. Zou, Y. Chen, Y. Wang, C. Cong, W. Huang, and T. Yu, Electrically tunable valley-light emitting diode (vled) based on cvd-grown monolayer ws₂, *Nano Letters* **16**, 1560–1567 (2016).

[41] G. Swain, G. J. Choi, J. S. Gwag, and Y. Kim, Monolayer mos2 and ws2 for vertical circular- polarized-light-emitting diode: from fundamental understanding to device architecture, *Advanced Electronic Materials* **11**, 10.1002/aelm.202400381 (2024).

[42] K. R. Hansen, J. S. Colton, and L. Whittaker-Brooks, Measuring the exciton binding energy: Learning from a decade of measurements on halide perovskites and transition metal dichalcogenides, *Advanced Optical Materials* **12**, 10.1002/adom.202301659 (2023).

[43] A. Ramasubramaniam, Large excitonic effects in monolayers of molybdenum and tungsten dichalcogenides, *Physical Review B* **86**, 10.1103/physrevb.86.115409 (2012).

[44] H. Shi, H. Pan, Y.-W. Zhang, and B. I. Yakobson, Quasiparticle band structures and optical properties of strained monolayer mos2 and ws2, *Physical Review B* **87**, 10.1103/physrevb.87.155304 (2013).

[45] G. Wang, I. C. Gerber, L. Bouet, D. Lagarde, A. Balocchi, M. Vidal, T. Amand, X. Marie, and B. Urbaszek, Exciton states in monolayer mose2 : impact on interband transitions, *2D Materials* **2**, 045005 (2015).

[46] D. Y. Qiu, F. H. da Jornada, and S. G. Louie, Screening and many-body effects in two-dimensional crystals: Monolayer mos2, *Physical Review B* **93**, 10.1103/physrevb.93.235435 (2016).

[47] H. Yu, M. Laurien, Z. Hu, and O. Rubel, Exploration of the bright and dark exciton landscape and fine structure of mos2 using gwo-bse, *Physical Review B* **100**, 125413 (2019).

[48] T. Ketolainen, N. Macháčová, and F. Karlický, Optical gaps and excitonic properties of 2d materials by hybrid time-dependent density functional theory: Evidences for monolayers and prospects for van der waals heterostructures, *Journal of Chemical Theory and Computation* **16**, 5876–5883 (2020).

[49] M. Marsili, A. Molina-Sánchez, M. Palummo, D. Sangalli, and A. Marini, Spinorial formulation of the gw-bse equations and spin properties of excitons in two-dimensional transition metal dichalcogenides, *Physical Review B* **103**, 10.1103/physrevb.103.155152 (2021).

[50] Y.-C. Shih, F. A. Nilsson, and G.-Y. Guo, Electron energy loss spectra and exciton band structure of wse2 monolayers studied by ab initio bethe-salpeter equation calculations, *Physical Review B* **110**, 205417 (2024).

[51] T. Chowdhury, S. Chatterjee, D. Das, I. Timokhin, P. D. Núñez, S. Chatterjee, K. Majumdar, P. Ghosh, A. Mishchenko, and A. Rahman, Brightening of dark excitons in ws 2 via tensile strain-induced excitonic valley convergence, *Physical Review B* **110**, L081405 (2024).

[52] P. Hernández López, S. Heeg, C. Schattauer, S. Kovalchuk, A. Kumar, D. J. Bock, J. N. Kirchhof, B. Höfer, K. Greben, D. Yagodkin, *et al.*, Strain control of hybridization between dark and localized excitons in a 2d semiconductor, *Nature communications* **13**, 7691 (2022).

[53] A. M. Kumar, D. Yagodkin, R. Rosati, D. J. Bock, C. Schattauer, S. Tobisch, J. Hagel, B. Höfer, J. N. Kirchhof, P. Hernández López, *et al.*, Strain fingerprinting of exciton valley character in 2d semiconductors, *Nature Communications* **15**, 7546 (2024).

[54] S. B. Chand, J. M. Woods, E. Mejia, T. Taniguchi, K. Watanabe, and G. Grosso, Visualization of dark excitons in semiconductor monolayers for high-sensitivity strain sensing, *Nano Letters* **22**, 3087 (2022).

[55] A. Javed, M. Asif, and R. Ullah, Band gap crossover and symmetry breaking in strained monolayer mos2, *Materials Letters* **372**, 137066 (2024).

[56] J. Madéo, M. K. Man, C. Sahoo, M. Campbell, V. Pareek, E. L. Wong, A. Al-Mahboob, N. S. Chan, A. Karmakar, B. M. K. Mariserla, *et al.*, Directly visualizing the momentum-forbidden dark excitons and their dynamics in atomically thin semiconductors, *Science* **370**, 1199 (2020).

[57] P. Giannozzi, O. Baseggio, P. Bonfà, D. Brunato, R. Car, I. Carnimeo, C. Cavazzoni, S. De Gironcoli, P. Delugas, F. Ferrari Ruffino, A. Ferretti, N. Marzari, I. Timrov, A. Urru, and S. Baroni, Quantum espresso toward the exascale, *The Journal of chemical physics* **152** (2020).

[58] J. P. Perdew, K. Burke, and M. Ernzerhof, Generalized gradient approximation made simple, *Physical review letters* **77**, 3865 (1996).

[59] D. Hamann, Optimized norm-conserving vanderbilt pseudopotentials, *Physical Review B* **88**, 085117 (2013).

[60] M. J. Van Setten, M. Giantomassi, E. Bousquet, M. J. Verstraete, D. R. Hamann, X. Gonze, and G.-M. Rignanese, The pseudodojo: Training and grading a 85 element optimized norm-conserving pseudopotential table, *Computer Physics Communications* **226**, 39 (2018).

[61] T. Sohier, M. Calandra, and F. Mauri, Density functional perturbation theory for gated two-dimensional heterostructures: Theoretical developments and application to flexural phonons in graphene, *Physical Review B* **96**, 075448 (2017).

[62] S. Grimme, Semiempirical gga-type density functional constructed with a long-range dispersion correction, *Journal of computational chemistry* **27**, 1787 (2006).

[63] V. Barone, M. Casarin, D. Forrer, M. Pavone, M. Sambi, and A. Vittadini, Role and effective treatment of dispersive forces in materials: Polyethylene and graphite crystals as test cases, *Journal of computational chemistry* **30**, 934 (2009).

[64] A. Marini, C. Hogan, M. Grüning, and D. Varsano, Yambo: an ab initio tool for excited state calculations, *Computer Physics Communications* **180**, 1392 (2009).

[65] D. Sangalli, A. Ferretti, H. Miranda, C. Attaccalite, I. Marri, E. Cannuccia, P. Melo, M. Marsili, F. Paleari, A. Marrazzo, G. Prandini, P. Bonfà, M. O. Atambo, F. Affinito, M. Palummo, A. Molina-Sánchez, C. Hogan, M. Grüning, D. Varsano, and A. Marini, Many-body perturbation theory calculations using the yambo code, *Journal of Physics: Condensed Matter* **31**, 325902 (2019).

[66] C. A. Rozzi, D. Varsano, A. Marini, E. K. U. Gross, and A. Rubio, Exact coulomb cutoff technique for supercell calculations, *Phys. Rev. B* **73**, 205119 (2006).

[67] A. Guandalini, P. D'Amico, A. Ferretti, and D. Varsano, Efficient gw calculations in two dimensional materials through a stochastic integration of the screened potential, *npj Computational Materials* **9**, 44 (2023).

[68] R. W. Godby and R. J. Needs, Metal-insulator transition in kohn-sham theory and quasiparticle theory, *Phys. Rev. Lett.* **62**, 1169 (1989).

[69] A. Oschlies, R. W. Godby, and R. J. Needs, Gw self-energy calculations of carrier-induced band-gap narrowing in n-type silicon, *Phys. Rev. B* **51**, 1527 (1995).

[70] G. Strinati, Application of the green's functions method to the study of the optical properties of semiconductors, *La Rivista del Nuovo Cimento (1978-1999)* **11**, 1 (1988).

[71] J. C. Smith and K. Burke, Interacting electrons: Theory and computational approaches, *American Journal of Physics* **85**, 636 (2017).

[72] R. M. Martin, L. Reining, and D. M. Ceperley, *Interacting electrons – Theory and Computational Approaches* (Cambridge University Press, 2016).

[73] P. Cudazzo, I. V. Tokatly, and A. Rubio, Dielectric screening in two-dimensional insulators: Implications for excitonic and impurity states in graphane, *Phys. Rev. B* **84**, 085406 (2011).

[74] G. Wang, A. Chernikov, M. M. Glazov, T. F. Heinz, X. Marie, T. Amand, and B. Urbaszek, Colloquium : Excitons in atomically thin transition metal dichalcogenides, *Reviews of Modern Physics* **90**, 10.1103/revmodphys.90.021001 (2018).

[75] J. Kunstmann, F. Mooshammer, P. Nagler, A. Chaves, F. Stein, N. Paradiso, G. Plechinger, C. Strunk, C. Schüller, G. Seifert, D. R. Reichman, and T. Korn, Momentum-space indirect interlayer excitons in transition-metal dichalcogenide van der waals heterostructures, *Nature Physics* **14**, 801–805 (2018).

[76] L. Debbichi, O. Eriksson, and S. Lebègue, Electronic structure of two-dimensional transition metal dichalcogenide bilayers from ab initio theory, *Physical Review B* **89**, 10.1103/physrevb.89.205311 (2014).

[77] R. Roldán, J. A. Silva-Guillén, M. P. López-Sancho, F. Guinea, E. Cappelluti, and P. Ordejón, Electronic properties of single-layer and multilayer transition metal dichalcogenides m x w ($m = \text{mo, w}$ and $x = \text{s, se}$), *Annalen der Physik* **526**, 347 (2014).

[78] R. Rodrigues Pela, C. Vona, S. Lubeck, B. Alex, I. Gonzalez Oliva, and C. Draxl, Critical assessment of g 0 w 0 calculations for 2d materials: the example of monolayer mos2, *npj Computational Materials* **10**, 77 (2024).

[79] Z. Khatibi, M. Feierabend, M. Selig, S. Brem, C. Lindnerälv, P. Erhart, and E. Malic, Impact of strain on the excitonic linewidth in transition metal dichalcogenides, *2D Materials* **6**, 015015 (2018).

[80] R. Rosati, S. Brem, R. Pereira-Causín, R. Schmidt, I. Niehues, S. Michaelis de Vasconcellos, R. Bratschitsch, and E. Malic, Strain-dependent exciton diffusion in transition metal dichalcogenides, *2D Materials* **8**, 015030 (2020).

[81] I. Niehues, R. Schmidt, M. Drüppel, P. Marauhn, D. Christiansen, M. Selig, G. Berghäuser, D. Wigger, R. Schneider, L. Braasch, R. Koch, A. Castellanos-Gomez, T. Kuhn, A. Knorr, E. Malic, M. Rohlfing, S. Michaelis de Vasconcellos, and R. Bratschitsch, Strain control of exciton-phonon coupling in atomically thin semiconductors, *Nano Letters* **18**, 1751–1757 (2018).

[82] B. Aslan, M. Deng, and T. F. Heinz, Strain tuning of excitons in monolayer wse2, *Physical Review B* **98**, 10.1103/physrevb.98.115308 (2018).

[83] H. Liu, L. Jiao, L. Xie, F. Yang, J. Chen, W. Ho, C. Gao, J. Jia, X. Cui, and M. Xie, Molecular-beam epitaxy of monolayer and bilayer wse2: a scanning tunneling microscopy/spectroscopy study and deduction of exciton binding energy, *2D Materials* **2**, 034004 (2015).

[84] K. Hao, J. F. Specht, P. Nagler, L. Xu, K. Tran, A. Singh, C. K. Dass, C. Schüller, T. Korn, M. Richter, *et al.*, Neutral and charged inter-valley biexcitons in monolayer mose2, *Nature communications* **8**, 15552 (2017).

[85] A. Raja, A. Chaves, J. Yu, G. Arefe, H. M. Hill, A. F. Rigos, T. C. Berkelbach, P. Nagler, C. Schüller, T. Korn, *et al.*, Coulomb engineering of the bandgap and excitons in two-dimensional materials, *Nature communications* **8**, 15251 (2017).

[86] B. Zhu, X. Chen, and X. Cui, Exciton binding energy of monolayer ws2, *Scientific reports* **5**, 9218 (2015).

[87] K. Wagner, J. Zipfel, R. Rosati, E. Wietek, J. D. Ziegler, S. Brem, R. Pereira-Causín, T. Taniguchi, K. Watanabe, M. M. Glazov, *et al.*, Nonclassical exciton diffusion in monolayer wse2, *Physical Review Letters* **127**, 076801 (2021).

[88] M. Tebyetekerwa, J. Zhang, Z. Xu, T. N. Truong, Z. Yin, Y. Lu, S. Ramakrishna, D. Macdonald, and H. T. Nguyen, Mechanisms and applications of steady-state photoluminescence spectroscopy in two-dimensional transition-metal dichalcogenides, *ACS nano* **14**, 14579 (2020).

[89] Y. Miyauchi, S. Konabe, F. Wang, W. Zhang, A. Hwang, Y. Hasegawa, L. Zhou, S. Mouri, M. Toh, G. Eda, *et al.*, Evidence for line width and carrier screening effects on excitonic valley relaxation in 2d semiconductors, *Nature Communications* **9**, 2598 (2018).

[90] A. V. Stier, N. P. Wilson, K. A. Velizhanin, J. Kono, X. Xu, and S. A. Crooker, Magneto-optics of exciton rydberg states in a monolayer semiconductor, *Physical review letters* **120**, 057405 (2018).

[91] G. Moody, K. Tran, X. Lu, T. Autry, J. M. Fraser, R. P. Mirin, L. Yang, X. Li, and K. L. Silverman, Microsecond valley lifetime of defect-bound excitons in monolayer wse2, *Physical review letters* **121**, 057403 (2018).

[92] A. V. Stier, N. P. Wilson, G. Clark, X. Xu, and S. A. Crooker, Probing the influence of dielectric environment on excitons in monolayer wse2: insight from high magnetic fields, *Nano letters* **16**, 7054 (2016).

[93] H. M. Hill, A. F. Rigos, C. Roquelet, A. Chernikov, T. C. Berkelbach, D. R. Reichman, M. S. Hybertsen, L. E. Brus, and T. F. Heinz, Observation of excitonic rydberg states in monolayer mos2 and ws2 by photoluminescence excitation spectroscopy, *Nano letters* **15**, 2992 (2015).

[94] M. Molas, A. Slobodeniuk, K. Nogajewski, M. Bartos, L. Bala, A. Babiński, K. Watanabe, T. Taniguchi, C. Faugeras, and M. Potemski, Energy spectrum of two-dimensional excitons in a nonuniform dielectric medium, *Physical Review Letters* **123**, 10.1103/physrevlett.123.136801 (2019).

[95] M.-H. Chiu, C. Zhang, H.-W. Shiu, C.-P. Chuu, C.-H. Chen, C.-Y. S. Chang, C.-H. Chen, M.-Y. Chou, C.-K. Shih, and L.-J. Li, Determination of band alignment in the single-layer mos2/wse2 heterojunction, *Nature Communications* **6**, 10.1038/ncomms8666 (2015).

[96] A. F. Rigos, H. M. Hill, K. T. Rim, G. W. Flynn, and T. F. Heinz, Electronic band gaps and exciton binding energies in monolayer moxw1-xs2 transition metal dichalcogenide alloys probed by scanning tunneling and optical spectroscopy, *Physical Review B* **94**, 10.1103/physrevb.94.075440 (2016).

[97] C. Zhang, A. Johnson, C.-L. Hsu, L.-J. Li, and C.-K. Shih, Direct imaging of band profile in single layer mos2 on graphite: Quasiparticle energy gap, metallic

edge states, and edge band bending, *Nano Letters* **14**, 2443–2447 (2014).

[98] T. Deilmann and K. S. Thygesen, Finite-momentum exciton landscape in mono- and bilayer transition metal dichalcogenides, *2D Materials* **6**, 035003 (2019).

[99] S. B. Chand, J. M. Woods, E. Mejia, T. Taniguchi, K. Watanabe, and G. Grosso, Visualization of dark excitons in semiconductor monolayers for high-sensitivity strain sensing, *Nano Letters* **22**, 3087–3094 (2022).

[100] M. R. Molas, C. Faugeras, A. O. Slobodeniuk, K. Nogański, M. Bartos, D. M. Basko, and M. Potemski, Brightening of dark excitons in monolayers of semiconducting transition metal dichalcogenides, *2D Materials* **4**, 021003 (2017).

[101] C. Robert, S. Park, F. Cadiz, L. Lombez, L. Ren, H. Tornatzky, A. Rowe, D. Paget, F. Sirotti, M. Yang, *et al.*, Spin/valley pumping of resident electrons in wse2 and ws2 monolayers, *Nature communications* **12**, 5455 (2021).